Probing Rotation of Core-collapse Supernova with Concurrent Analysis of Gravitational Waves and Neutrinos

Takaaki Yokozawa[1], Mitsuhiro Asano[1], Tsubasa Kayano[2], Yudai Suwa[3,4], Nobuyuki Kanda[1], Yusuke Koshio[2], and Mark R. Vagins[5,6]

ABSTRACT

When a core-collapse supernova (SN) happens in our galaxy, various detectors will detect gravitational waves (GWs) and neutrinos. Current numerical simulations have successfully introduced multi-dimensional effects to produce exploding SN models, but thus far the explosion mechanism is not well understood. In this paper, we focus on an investigation of progenitor core rotation via comparison of the start time of GW emission and that of the neutronization burst. The GW and neutrino detectors are assumed to be the KAGRA detector and EGADS detector, respectively. Our detection simulation studies show that for a nearby supernova(<0.2 kpc) we can confirm the lack of core rotation close to 100% of the time, and the presence of core rotation about 90% of the time.

Subject headings: supernovae:general, neutrinos, gravitational waves, stars:rotation

1. Introduction

Supernovae explosions are among the most energetic events in the universe. Core collapse supernovae are the final phase in the evolution of massive stars with $M \gtrsim 8M_\odot$. Most of the released gravitational energy, $\sim 10^{53}$ ergs, is emitted as neutrinos and only a small

[1]Graduate School of Science, Osaka City University, Sumiyoshi-ku, Osaka 558-8585, Japan

[2]Department of Physics, Okayama University, Okayama, Okayama, 700-8530, Japan

[3]Yukawa Institute for Theoretical Physics, Kyoto University, Oiwake-cho, Kitashirakawa, Sakyo-ku, Kyoto 606-8502, Japan

[4]Max-Planck-Institut für Astrophysik, Karl-Schwarzschild-Str. 1, 85748 Garching, Germany

[5]Kavli Institute for the Physics and Mathematics of the Universe(WPI), Todai Institutes for Advanced Study, University of Tokyo, Kashiwa, Chiba 277-8583, Japan

[6]Department of Physics and Astronomy, University of California, Irvine, Irvine, CA 92697-4575, USA

fraction ($\sim 1\%$, so $\sim 10^{51}$ ergs) is used to produce the violent explosion itself (Bethe 1990). Although the historic detection of neutrinos from SN 1987A (Hirata et al. 1987; Bionta et al. 1987; Alekseev et al. 1987) validated our basic picture of core collapse (e.g. the total energy, the emission timescale of neutrinos, etc.), there are still large unceainties concerning the explosion mechanism itself. In addition to photons and neutrino observations, the next nearby (probably galactic) supernova will also likely be observed using a relative newcomer to multi-messenger astronomy, namely gravitational waves (GWs). Owing to their weak coupling with matter they have the potential to provide us with information about the innermost part of these violent phenomena, and hence could serve as a unique window into the explosion mechanism (see Ott 2009; Kotake et al. 2012, and references therein). The new multi-messenger astronomy era will include observation of broad-band photons (from radio to gamma), multi-energy neutrinos (from MeV to PeV), and multi-frequency GWs (from Hz to kHz) using various telescopes and detectors already in operation as well as those coming online in the near future. Using these signals we can see different aspects of astronomical objects. What's more, after decades of effort recent developments in the numerical simulation of core-collapse supernovae are making remarkable progress: there are several simulation studies showing successful shock expansion (see Sec. 2.). In light of these facts, we will give some prospects of what we can learn from the next nearby core-collapse supernova, especially focusing on the presense of rotation, so crucial for a variety of explosion mechanism candidates.

In this study, we employ theoretical predictions of self-consistent signals of neutrinos and GWs based on recent simulations of multi-dimensional neutrino-radiation hydrodynamics (e.g., Suwa et al. 2010). By considering realistic detector simulation that consists of not only responses for both GWs and neutrinos but also takes into account noise and statistical behavior, we investigate the feasibility of extracting information concerning the most crucial period in the death of massive stars. We define characteristic times: epoch time of GW $\mathcal{T}_{GW}$ and of neutronization burst $\mathcal{T}_{\nu}$. Supposing that the core rotates rapidly, the GW would be detectable prior to neutronization burst (i.e. $\mathcal{T}_{GW} < \mathcal{T}_{\nu}$) and vice versa (see Pagliaroli et al. 2009; Halzen & Raffelt 2009, for time determination of core bounce by neutrinos alone).

For our canonical GW detector we use KAGRA, which is currently under constraction (Aso et al. 2013), and for our neutrino detector we use EGADS, which is now operating (Mori 2013). This is because (i) the neutronization burst generates copious amount of electron-type neutrinos, so the gadolinium-loaded EGADS would be more suitable than the larger Super-Kamiokande[1](Ikeda et al. 2007), and (ii) since both KAGRA and EGADS detectors

---

[1]Here we neglect neutrino oscillation effects for simplicity.

are located in the same place, i.e. the Kamioka mine, signal travel time between detectors does not have to be taken into account.

Section 2 describes the numerical simulation and supernova signals which are used in this analysis. Section 3 describes the characteristics of KAGRA and EGADS detectors. Section 4 shows the method of time extraction of $\mathcal{T}_{GW}$ and $\mathcal{T}_{\nu}$, with the result of determining the probability of progenitor core rotation. Finally, Section 5 contains a summary and discussion of our results.

2. Numerical Simulation of Core-collapse Supernova

In this section, we illustrate the numerical simulation of core-collapse supernova explosions. First, we shortly explain the basics of simulations. Secondly, numerical methods used in this study are given. Thirdly, hydrodynamic features are expressed, and finally neutrino and gravitational wave emissions are presented.

2.1. Basics

Since there are various types of physics involved in core-collapse supernova explosions, detailed numerical simulations are indispensable. For instance, gravity describes how the matter collapses and how much energy is released during the collapse. In addition, a final outcome of supernovae are neutron stars (NSs), so that the nuclear force, which determines the structure of a NS, is critically important. Neutrino interaction rates, which give the cooling rates of the core as well as heating rates of post-shock material by neutrino absorption (this will be explained later), are treated in great detail to give a quantitatively correct answer. This is because the total amount of neutrino emission is $\sim 10^{53}$ erg, while the explosion energy itself is $\sim 10^{51}$ erg, therefore only a few percent of energy deposition by neutrinos can drive the explosion; indeed, this is the so-called standard scenario of core-collapse supernovae (see Bethe & Wilson 1985 for original idea and Kotake et al. 2012; Janka 2012; Burrows 2013 for recent reviews). The electromagnetic interaction also plays an important role because the system consists of fully-ionized plasma, and so Coulomb scattering allows us to treat the stellar matter as if it were in the fluid state.

Due to the complexity of the system, we have not achieved fully consistent explosions using simulation thus far. However, several exploding simulations arising from the neutrino heating mechanism have been reported in the last decade (Buras et al. 2006; Marek & Janka

2009; Suwa et al. 2010; Müller et al. 2012; Takiwaki et al. 2012; Bruenn et al. 2013).[2] These simulations exhibited smaller explosion energy, i.e., $\sim 10^{49}$–10^{50} ergs, than the observationally required value, $\sim 10^{51}$ ergs, leading to continuous accretion onto a NS beyond the maximum supportable mass, inevitably resulting in an eventual collapse to a black hole instead of a NS. More recently, although the small explosion energy problem remains, there has been a *successful* exploding simulation, which means the mass accretion onto a NS ceases and the final mass eventually settles into $\sim 1.3 M_\odot$, by Suwa (2014) using a progenitor with 11.2 $M_\odot$ at zero-age main sequence phase. This explosion is a consequence of a steep density gradient between the Si and O layers, which results in a rapid decrease of the mass accretion rate onto the shock wave (Suwa et al. 2014). After this shell passes through the shock, the shock begins to expand and the system eventually produces the explosion. In this study, we use the same progenitor and the same simulation code.

2.2. Methods

The numerical methods used in this study are the same as Suwa et al. (2010, 2011, 2013, 2014); Suwa (2014). In this code, we solve neutrino radiation hydrodynamic equations, which consist of hydrodynamic equations and neutrino radiative transfer equation (see Suwa et al. 2013 for more details). The nuclear equation of state employed is Lattimer & Swesty (1991) with the incompressibility parameter of $K = 220$ MeV. As for the initial condition, we employ $11.2 M_\odot$ model from Woosley et al. (2002), which was used in several previous works.

The rotation is imposed with shellular rotation law as

$$\Omega(r) = \Omega_0 \frac{r_0^2}{r^2 + r_0^2}, \tag{1}$$

where $\Omega(r)$ is an angular velocity with r being the radius from the center, Ω_0 is the angular velocity at the center, and r_0 is a radius that determines the degree of differential rotation. Here, we employ $r_0 = 1000$ km. In order to investigate how the rotation affects emissions of gravitational waves and neutrinos, we perform simulations with different rotation strengths of $\Omega_0 = 0.0\pi$, 0.2π, 0.5π, and 1.0π radian s^{-1}.

In this paper, we evaluate the gravitational wave emission from aspherical motion of fluids via the Newtonian quadrupole formulae of Mönchmeyer et al. (1991). We do not

---

[2]Note that some simulations of multi-dimensional neutrino radiation hydrodynamics also reported the failure of the explosion by neutrino heating (Burrows et al. 2006; Ott et al. 2008; Hanke et al. 2013; Dolence et al. 2014), so that this mechanism still contains ambiguities.

discuss the gravitational wave emission from anisotropic neutrino emission (Epstein 1978; Burrows & Hayes 1996; Mueller & Janka 1997) because this component contributes to GW at later time and does not affect GW around the bounce time.

2.3. Hydrodynamic Features

After the simulation sets in, the gravitational collapse begins and the central density increases. Around 180 ms, the central density reaches the nuclear density ($\sim 3 \times 10^{14}$ g cm^{-3}), which indicates the formation of a protoneutron star (PNS). The equation of state becomes much stiffer above this density so that the infall of material ceases and a shock wave is produced at the surface of the PNS. This shock propagates outward initially, but loses its energy due to the photodissociation of iron and neutrino emission so that it decelerates. About 100 ms after the bounce, which is defined here by the time of the maximum central density, the shock expands again owing to the neutrino heating mechanism. All simulations used in this study result in explosion, i.e., we observe the shock expansion above a few thousands km. As for the nonrotating model, Suwa et al. (2013) and Suwa (2014) give more information, which are valid even for rotating models of this paper, since the rotation is not too strong to change the whole picture.

2.4. Neutrinos and Gravitational Waves

Figure 1 represents the time evolution of luminosities of electron-type neutrinos (ν_e; panel (a)) and antineutrinos ($\bar{\nu}_e$; panel (b)), respectively. One can see the general trend does not depend on the initial rotation rate very much. In the first few tens of ms for ν_e, there is the so-called neutronization burst, which is generated by the rapid absorption of electrons by protons (electron capture; $e + p \rightarrow n + \nu_e$) in the regime between the shock and PNS, causing emission of large amounts of ν_e. After that the neutrino luminosity is gradually decreasing, but a large luminosity is still observed. On the other hand, $\bar{\nu}_e$ does not have such a spiky structure due to lack of positrons before bounce. Both ν_e and $\bar{\nu}_e$ exhibit that only the fastest rotation model ($\Omega_0 = 1.0\pi$ rad s^{-1}) results in slightly smaller luminosity due to stronger centrifugal force and slower contraction of the PNS, while slower rotation models share similar, minimally-affected characteristics as compared to the non-rotating case. Therefore, we can argue that the currently employed rotation strength does not significantly change the generic picture about neutrinos.

Figure 2 depicts the time evolution of the gravitational wave signal. Note that in the

early phase the gravitational wave strength strongly depends on the initial rotation (see small panel). As for models without rotation and with slow rotation, the density structure is almost spherically symmetric so that there is no or only small GW emission. On the other hand, the strongly rotating model exhibits strong GW emission at the time of bounce because the centrifugal force makes the core asymmetric. Therefore, we can constrain the rotation strength by detecting GW at just the time of bounce. We can constrain the bounce time in turn using neutrino data as shown in Fig. 1, in which we show that the neutrino emission does not depend on the rotation strength so that neutrinos are a guaranteed signal from core-collapse supernova.

3. Detectors

In this section, we introduce the KAGRA and EGADS detectors, which are used to determine progenitor core rotation in this paper.

As described in the introduction, one of the important benefits of employing EGADS and KAGRA is the close proximity of these two detectors. This makes it possible to avoid any significant time-lag in arrival times of gravitational wave and neutrino signals due to distance between the detectors. In gravitational wave detection, the angular resolution of the source direction is not as good as that of optical telescopes, even in multiple-detector observations. According to the diffraction limit of wavelength ($\sim$300 km for 1 kHz) and interval of detectors ($\sim$1000 km), typical angular resolution for the kHz band burst wave is only a few degrees (Grover et al. 2014). Water Cherenkov detectors have a similar, few-degree angular resolution for supernova explosions $\sim$ 10kpc away (i.e., near the galactic center) (Ando & Sato 2002; Tomàs et al. 2003). These facts mean that the correction of arrival time based on direction for well-separated detectors will have a larger error than the timing accuracy which is required in this paper study, $<$ 1 msec, for neutrino and gravitational wave signals only. Closely placed detectors do not suffer from this problem.

3.1. KAGRA Detector

KAGRA is a laser interferometric gravitational wave detector which is being constructed in the Kamioka mine in Gifu, Japan (Kuroda & the LCGT Collaboration 2010). The KAGRA interferometer consists of two 3 km base-line laser cavity arms; all optical and vacuum systems are located inside a mountain, providing a silent and stable environment. KAGRA will employ cryogenic mirrors made of monolithic crystals of sapphire to reduce the thermal

noise. Its target sensitivity is a few $\times 10^{-24}$ $[1/\sqrt{\text{Hz}}]$ in strain 'h' of the space-time metric around 100 Hz (Aso et al. 2013). [3] There are other gravitational wave detectors which will have similar sensitivity, i.e. LIGO in the US (Abbott et al. 2009) and Virgo in Europe (Accadia et al. 2011). Their upgraded configurations [4] [5] and a global observation network of four gravitational wave detectors are expected to be in operation in late 2017 or 2018.

The basic concept of the laser interferometric gravitational wave detector is based on a 'Michelson' interferometer, otherwise known as a 'free mass' type detector. It measures the space-time strain h by determining the travel time of light between test masses. Instead of a free falling test mass, detectors of this type employ suspended high-quality mirrors. The suspension is not only to maintain the mirrors as 'free masses' in a higher frequency band, but also as a mechanical filter that isolates disturbances from outside. Coherent laser light will be directed down two right-angled base-line arms. To integrate strain distortion, each arm serves as a long base-line and hi-finesse Fabry-Perot cavity that consists of two mirrors. Since gravitational waves are quadrupole waves, differential motion of these mirrors is expected in case of azimuthal incidence. Thus, returning light from the two arms will experience a relative phase difference when gravitational waves are passing by. The detector measures the interference of the two beams as a highly sensitive test of the presence of impinging gravitational waves.

To achieve these detectors' high sensitivity various things are required: a long baseline to integrate strain effect, a high-power laser to protect against quantum shot noise, high-quality and heavy mirrors, a vacuum system to eliminate air fluctuations, many advanced technique of optics including quantum optics, and so on. KAGRA employs special techniques, particularly in its underground site and cryogenic mirrors.

These gravitational wave detectors are aiming for the first ever observation of gravitational waves having astrophysical origins. Promising candidates are coalescence of compact star binaries consisting of neutron stars or black holes up to 100 Mpc away, rotating pulsars in our own galaxy, and stellar core-collapse supernova explosions both in our own and in neighboring galaxies.

---

[3]KAGRA official sensitivity (http://gwcenter.icrr.u-tokyo.ac.jp/researcher/parameters)

[4]aLIGO ; https://www.advancedligo.mit.edu/

[5]aVirgo ; https://wwwcascina.virgo.infn.it/advirgo/

3.2. EGADS Detector

The EGADS (originally standing for Evaluating Gadolinium's Action on Detector Systems) detector (Mori 2013) is a gadolinium (Gd) loaded water Cherenkov detector initially built as a demonstrator for GADZOOKS! (Beacom & Vagins 2004), the proposal to load Super-Kamiokande (SK) with a water-soluble gadolinium salt. EGADS is located in the Kamioka mine which is in the same mountain as both SK and KAGRA.

GADZOOKS! envisions adding 0.2% by mass of gadolinium sulfate $(Gd_2(SO_4)_3)$ into SK in order to facilitate the efficient detection of neutrons from Inverse Beta Decay (IBD) reactions $(\bar{\nu}_e + p \rightarrow e^+ + n)$. Gadolinium has the highest capture cross section for thermal neutrons of any naturally occuring substance, and emits an 8.0 MeV gamma cascade following capture. This can be easily detected in water Cherenkov detectors like SK, making neutrons visible and thereby tagging up to 90% of the IBD events as genuine due to the coincidence in both time ($\sim$30 ms) and space ($\sim$1 meter) between the prompt positron and the delayed gadolinium neutron capture cascade (Watanabe et al. 2009).

This detector consists of a cylindrical stainless steel tank, whose height and radius are 6.7 m and 6.5 m, respectively. A total of 240 inward-facing photodetectors line the inner walls of the EGADS tank. Most of these ($\sim$90%) are SK-style 50-cm diameter photomultiplier tubes (PMTs), while the rest are prototype light detectors of various sizes and designs being considered for use in the future Hyper-Kamiokande project (Abe et al. 2011). The resulting active light collecting surface area in EGADS is 40%, the same as in SK. The EGADS tank contains a total of 200 tons of Gd loaded water, about 100 tons of which is in front of the PMTs.

Following the R&D phase of operations (2010-2014), EGADS has been repurposed as a dedicated supernova neutrino detector, with the acronym now standing for Employing Gadolinium to Autonomously Detect Supernovae. Deadtime-free front-end electronics (Nishino et al. 2009) have been purchased, the same type used in SK since 2008, and will be installed in EGADS in 2015. From that point on the detector will run continuously as a supernova neutrino detector with realtime online event reconstruction.

The power of the neutron tagging made possible by gadolinium loading will allow EGADS to be a very capable supernova detector indeed, as the distinctive "gadolinium heartbeat" - the double pulse of positron and neutron capture gamma cascade - will instantly identify any galactic supernova as genuine (Adams et al. 2013). By allowing event-by-event tagging of the copius IBD events, they may be subtracted away from other, rarer signals. This yields a variety of additional advantages, potentially including improved determination of the supernova's position in the sky, as well as identification of the early neutronization

burst.

In addition to lacking effective neutron tagging, SK cannot record all of the data produced by nearby supernovae (Yokozawa 2011). By contrast, EGADS will have not only highly efficient tagging but also full supernova sensitivity for the entire Milky Way galaxy; it would expect to record about 40 events for a core-collapse explosion at the galactic center and 100,000 events for an explosion at the distance of Betelgeuse.

4. Detection Simulation

In this section we describe the detector signal simulation for KAGRA and EGADS, and the method of how to determine progenitor core rotation from these detectors. The analysis path is as follows: (i) Run supernova detection simulation with KAGRA and EGADS detector, respectively. (ii) Extract the epoch time of GW, $\mathcal{T}_{GW}$, and neutronization burst, $\mathcal{T}_{\nu}$. (iii) Compare these times and determine rotation or not. (iv) Loop 10,000 times and evaluate P_r, which is the probability to of core rotation. The initial angular momentum of progenitor core rotation in the supernova models are given several different magnitudes: $\Omega_0 = 0.0\pi$, 0.2π, 0.5π and 1.0π rad s^{-1}. The distance to the SN is chosen to be uniformly distributed between 0.1 to 2.0 kpc. The incident direction strongly affects GW detector response, but has little bearing on neutrino detection.

4.1. GW Analysis

4.1.1. Detector Signal

The output signal of the interferometric detector, $s(t_i)$, will be sampled with finite frequency $1/\delta t$, and can be written as

$$s(t_i) = h(t_i) + n(t_i), \qquad (2)$$

where $i=0,1,2,..$ is sample index and $h(t_i)$ is gravitational signal from supernova with beam pattern, polarization of GW emission, and distance from the sources taken into account. The 16,384 Hz sampling frequency of the KAGRA detector is used. $n(t_i)$ is time domain of detector noise.

When generating $n(t_i)$, we assume stationary and Gaussian detector noise of the KAGRA detector. Figure 3 shows the sensitivity curve of bKAGRA detector (Aso et al. 2013). After randomly fluctuating Gaussianity in the frequency domain, we apply Inverse Fourier Transform.

The detector's response for the long wavelength approximation, where the arm length of the detector is smaller than the reduced wavelentgh $\lambda/2\pi$, can be described with detector coordinates (latitude λ, longitude L, angle between East and bisector of the detector arms γ, angle between detector arms ζ), GW source coordinates (right ascension α, declination δ, inclination angle from symmetric axis ι in 2D numerical simulation model), local sidereal time of the detector's site $\phi_t+\Omega_r t$, and polarization angle Φ. These effects can be written as beam-pattern functions, F_+, $F_\times$. Using an axisymmetric explosion model, the inclination angle between $+Z_w$ axis should be taken into account. The detailed calculation is done in Jaranowski et al. (1998). In case of a gravitational wave emitted from the light source traveling in the $+Z_w$ direction, the signal h can be written with two independent waves' polarizations. That is, the simulated detector signal is written as follows;

$$s_{det}(t) = F_+(\alpha, \delta, \phi, \theta, \phi_r, t_i)h_+(r, \iota, t_i) + F_\times(\alpha, \delta, \phi, \theta, \phi_r, t_i)h_\times(r, \iota, t_i) + n_{det}(t_i). \qquad (3)$$

The KAGRA detector's coordinates are summarized in Table 1.

4.1.2. Calculation of Signal to Noise Ratio

To evaluate signal and noise power from obtained $s_{det}(t)$, the Excess Power Filter (Anderson et al. 2001) and Short Time Fourier Transform (STFT) are used. The Excess Power Filter extracts signal power with given time $[t_s, t_s+\Delta t]$, where t_s and Δt are a start time and a time duration of STFT data, respectively, in a frequency band $[f_s, f_s+\Delta f]$. In this paper, the duration time Δt is fixed at 31.25 ms and the frequency band is [40,5000] Hz. We remove the peak frequency of thermal suspension noise when extracting signal power.

The simulated signal is whitened via a FIR whitening filter to flaten the noise spectrum in the frequency domain. The whitened signal $\tilde{S}_w(f)$ is calculated by

$$\tilde{S}_w(t_s, f) = \frac{\tilde{S}(t_s, f)}{\langle \tilde{N}(f) \rangle}, \qquad (4)$$

and $\tilde{S}(t_s, f)$ is calculated by

$$\tilde{S}(t_s, f) = \int_{t_s}^{t_s+\Delta t} s_{det}(t')W(t' - t_s)\exp(-2\pi i f t')dt', \qquad (5)$$

where $\langle \tilde{N}(f) \rangle$ is obtained from the running median (Mohanty 2002) of simulated noise data, and $W(t)$ is a Hann window function.

The signal power P_s and Signal to Noise Ratio (SNR) can be defined as follows:

$$P_s(t_s) = \sqrt{\frac{\int \tilde{S}_w^*(t_s, f) \cdot \tilde{S}_w(t_s, f) df}{\int \langle \tilde{N}_w^*(f) \cdot \tilde{N}_w(f) \rangle df}}, \tag{6}$$

$$SNR(t_s) = \frac{P_s(t_s) - m}{\sigma}, \tag{7}$$

where m and σ are the normalized mean and deviation of $P_n = \sqrt{\int \tilde{N}_w^*(f) \cdot \tilde{N}_w(f) df}$ distribution, respectively. To obtain m and σ we first evaluate the noise behavior, without injecting a supernova signal, and evaluate P_n. The noise distribution shows $m=1$ and $\sigma=0.06$.

4.1.3. Extracting Start Time of GW Emission

The center of the timing window which contains the local maximum SNR ($t_s|_{\text{max SNR}}$ + 15.625[s]) is defined as $\mathcal{T}_{GW}$, the start time of GW emission. Figure 4 shows one example of the time variation of obtained SNR for each rotation model. The supernova distance is set to an on-direction 1.0 kpc for the KAGRA detector. In this case, each supernova simulation gives $\mathcal{T}_{GW}$ values of 33 ms(0.0π rad s^{-1}, magenta), 23 ms(0.2π rad s^{-1}, green), 18 ms(0.5π rad s^{-1}, blue) and 0 ms(1.0π rad s^{-1}, red), respectively.

Figure 5 shows the local maximum SNR distribution after running each model 10,000 times. In this figure, the supernova distance is set to 1.0 kpc. The SNR value is larger for stronger core rotation models because stronger amplitude GW's are emitted for stronger core rotation models. We define the detection threshold for GW analysis as local maximum SNR > 8 (black line). This threshold corresponds to a False Alarm Ratio of $\sim 10^{-6}$ per year.

Figure 6 and Fig. 7 show the $\mathcal{T}_{GW}$ distributions for each explosion model after applying this detection criterion (local maximum SNR > 8). The supernova distances from Earth are set to 0.1 kpc or 1.0 kpc. The horizontal axis shows the time after core bounce, when the central progenitor core density becomes maximum. When the progenitor core is strongly rotating, $\mathcal{T}_{GW}$ is almost the same time as core bounce, with sharper distributions for closer supernova explosions. Unfortunately, due to the second peak of $h(t)$ in the 1.0π rad s^{-1} model which can be found around 16 ms in Figure 2, some simulations show mis-identification of core bounce time.

4.1.4. Model Dependence

To evaluate the uncertainty of GW epoch extraction we apply the same analysis to supernova models provided by Dimmelmeier et al. (2008). Of these, we select the single centrifugal bounce models, which are marked with crosses in their Table III, because we are interested in fast rotating models. There are 25 models under this classification.

One example of the Dimmelmeier model for gravitational wave amplitude $h_{Dim}(t)$ and the time evolution of the maximum density $\rho_{Dim,max}(t)$ is shown in Fig. 8. This model is called 'e20b-ls'; the progenitor mass is 20 $M_\odot$ and the initial state is given by stellar evolution simulation.

Figure 9 and Fig. 10 show the detection efficiency and mean value of extracted time distributions when applying SNR >8 for the Dimmelmeier models. For all such models, the extracted times are within about -1±2 ms before core bounce. This result means that for strong GW models we can extract GW emission time with a few ms uncertainty.

4.2. Neutrino Analysis

Now we will present our method for estimating time variation of the expected number of neutrino interactions and extraction of neutronization burst time.

As an aside, we would like to discuss the effect of neutrino mass on neutrino speed. If the neutrino mass is assumed to be 0.1 meV, derived from the current direct observational limit, cosmological limit (Komatsu et al. 2011), and neutrino-less double beta decay experiment limit(Gando et al. 2012), the latency versus light speed is of order 0.1 ms for an explosion at the center of the galaxy. Thus, the mass of neutrinos does not affect the following discussion.

As a further simplification to the analysis, we do not take neutrino oscillation effects into account, and only consider the electron flavor neutrino interactions while neglecting those of the μ, and τ flavor neutrinos.

4.2.1. Expected Number of Interactions in EGADS

From neutrino luminosity, $L_\nu(t)$, and mean energy, $\langle E_\nu(t)\rangle$ of Fig. 1, we obtained an energy distribution, $dn/dE(t)$, assuming a Fermi-Dirac distribution

$$\langle E_\nu(t)\rangle = \frac{F_3}{F_2}T(t) \approx 3.15T(t),$$

$$f(E,t) = \frac{E^2}{1 + \exp(E/T(t))},$$

$$\frac{dN}{dE(t)} = f(E,t) \times \frac{L_\nu}{F_3 T^4 (4\pi r^2)}, \tag{8}$$

where $T(t)$ is absolute temperature for given time, r is distance from Earth, and F_2 and F_3 is defined as

$$F_k = \int_0^\infty \frac{x^k}{1 + \exp(x)},$$

$$F_2 \approx 1.803,$$

$$F_3 \approx 5.683. \tag{9}$$

To identify the time of the neutronization burst, the expected event rate must be obtained. We consider three types of interactions in EGADS. The first one is electron neutrino-electron elastic scattering,

$$\nu_e + e \rightarrow \nu_e + e. \tag{10}$$

This is the primary interaction with which to identify the neutronization burst. The cross section of the reaction is described in Bahcall et al. (1995). The second one is electron anti-neutrino elastic scattering,

$$\bar{\nu}_e + e \rightarrow \bar{\nu}_e + e. \tag{11}$$

The cross section is also described in Bahcall et al. (1995). Because this reaction occurs only in neutral current interactions, the cross section is six times smaller than that of electron scattering (Eq. 10), but this interaction will be a background of the neutronization burst search. The final one is inverse beta decay,

$$\bar{\nu}_e + p \rightarrow e^+ + n. \tag{12}$$

The cross section is described in Totani & Sato (1995). The gadolinium-loaded EGADS detector has the ability to separate inverse beta decay reactions from other reactions via tagging of the follow-on neutron. Because neutron tagging efficiency is roughly 90%, 10% of these interactions remain as background.

There are other events generated by supernova neutrinos in water Cherenkov detectors, such as (i) Neutrino-Oxygen interactions, (ii)μ, τ neutrino-electron elastic scattering, and so on. But the rates of these interaction will be small, so that we do not take them into account in the following analysis. Also, because the duration of a neutronization burst is ~ 10 seconds, the detector background may also be ignored ($\sim 10^{-6}$ events s^{-1}).

Figure 11 shows the expected number of these three interactions in EGADS in the case of a supernova explosion near the center of our galaxy for the model with $\Omega_0 = 1.0\pi$ rad

s^{-1}. Figure 12 shows the progenitor core rotation dependence of expected interaction rates. If the progenitor core is strongly rotating, the gravitational energy is released by rotation, in which case the neutrino luminosity becomes smaller as compared with weaker rotation models.

We employ Poisson statistics to represent the fluctuation of the observed number of neutrinos within 1 ms intervals. Figure 13 shows one example of the time fluctuation of observed neutrinos for for the model with $\Omega_0 = 1.0\pi$ rad s^{-1}. The distances are set to 0.1 kpc (red) and 0.5 kpc (blue).

4.2.2. Extracting Neutronization Burst Time

The neutronization burst time, $\mathcal{T}_\nu$, is obtained via the following steps: (i) Open 6 ms sliding window. (ii) Count the number of observed neutrinos. (iii) Shift 1 ms and calculate again. (iv) If maximum observed number of neutrinos exceeds three events, we define this to be an observation of the neutronization burst. (v) The left edge which gives maximum observed number of neutrinos is defined as $\mathcal{T}_\nu$. If there are multiple candidates for $\mathcal{T}_\nu$, the most left timing window is defined as $\mathcal{T}_\nu$. Figure 14 shows the maximum observed number of neutrinos for each rotation model. As already shown in Fig. 12, the model dependence is small.

Figure 15 shows the $\mathcal{T}_\nu$ distributions for the 1.0π rad s^{-1} model at 0.1 kpc, 0.5 kpc, and 1.0 kpc. For the 0.1 kpc case, the resulting $\mathcal{T}_\nu$ distribution is quite narrow, and the $\mathcal{T}_\nu$ is estimated as expected. But as the supernova distance becomes greater, the number of observed neutrinos becomes smaller, proportional to r^{-2} with r being the distance. Therefore, the $\mathcal{T}_\nu$ distribution fluctuates, and statistical uncertainties become larger with increasing distance to the burst.

4.3. Coincidence Analysis

4.3.1. Definition of Progenitor Core Rotation Probability

By comparing two parameters, $\mathcal{T}_{GW}$ and $\mathcal{T}_\nu$, we will able to acertain the probablility that the progenitor's core was rotating at the time of collapse.

Figure 16 and Fig. 17 show the distributions of $\mathcal{T}_{GW}$ and $\mathcal{T}_\nu$ for the 0.0π rad s^{-1} and 1.0π rad s^{-1} models. The distance is fixed at 0.1 kpc. Except for a minor peak in the $\mathcal{T}_{GW}$ distribution for 1.0π rad s^{-1} model, a simple comparison between these two times seems to

be enough for discussion of progenitor core rotation. So, the definition of progenitor core rotation is as follows: we calculate t_c which is defined as

$$t_c = \mathcal{T}_{GW} - \mathcal{T}_\nu, \tag{13}$$

and if $t_c <0$, we suppose progenitor core rotation, while for $t_c >0$, we suppose NO core rotation.

4.3.2.   Results

Figure 18 shows the distance dependence of P_r for each progenitor core rotation model, where P_r is defined as the probability of core rotation when both GW and neutronization burst signals have been observed. Once again, each color represents different progenitor core rotation models – 0.0π(magenta), 0.2π(blue), 0.5π(green) and 1.0π(red) rad s^{-1}, respectively. From Fig. 18, we have obtained these conclusions:
(1) For weakly rotating models (0.0π, 0.2π, 0.5π rad s^{-1}), the P_r value is expected to be close to 0%. In the near distance cases (0.1 and 0.2 kpc) the P_r value is almost 0 as expected. But in the far distance (>0.5 kpc) the P_r value becomes larger because of growing statistical uncertainty on the number of observed events, which leads in turn to reduced determination accuracy of the neutrinization burst time ($\mathcal{T}_\nu$) as shown in Fig. 15.
(2) For the strongly rotatng model (1.0π rad s^{-1}), the P_r value is as expected close to 100%. But, as shown in Fig. 7, there are two peaks due to mis-identifying T_{GW}. This makes for a lower P_r for the far distance. Still, even for the 2.0 kpc case the P_r value exceeds 70%.

The GW and neutronization burst detection probability and P_r for each progenitor core rotation model are summarized in Table 2 to Table 5.

5.   Summary and Discussion

By using a consistent supernova explosion model emitting both GWs and neutrinos, we investigate the progenitor core rotation to compare the GW emission start time, $\mathcal{T}_{GW}$, obtained from KAGRA detector, and neutronization burst time, $\mathcal{T}_\nu$, which is obtained from EGADS detector. The results show if a nearby supernova is very close(<0.2 kpc), we can correctly determine NO core rotation about 100% of the time if the progenitor core is indeed NOT rotating, and determine the presence of core rotation about 90% if the progenitor core is strongly rotated. But we investigate only nearby supernovae using only a single GW and

neutrino detector for this analysis.

For the problem as to why only nearby supernovae are useful, the main reason is due to the fact that the number of observed neutrinos is proportional to $1/r^2$. If the GADZOOKS! project starts, we can do same analysis with the SK volume in place of the EGADS volume (an increase from 100 tons to 22.5 ktons). In such a case, the detection efficiency of the neutronization burst is calculated to be about 96% for an explosion at the galactic center (10 kpc). Furthermore, a coherent or coincidence analysis using multiple GW detectors would help to improve the detection efficiencies. Beyond these potential points for improvement, we currently investigate progenitor core rotation with only two parameters, $\mathcal{T}_{GW}$ and $\mathcal{T}_{\nu}$. Applying multiple classification analysis, the accuracy of P_r is expected to be improved. These things represent our next homework.

Next, we comment on the limitations of our numerical model. First, we employed numerical results of two-dimensional (axisymmetric) Newtonian hydrodynamic simulation of a core-collapse supernova. It is well known that the hydrodynamic features between 2D and 3D are different, especially for the cascade direction of turbulent motion (Hanke et al. 2012; Couch & O'Connor 2014; Handy et al. 2014; Takiwaki et al. 2014). However, we do not expect our conclusion to be affected significantly because in this study we concentrated on the early phase (several 10 ms). More important limitations of this study are neglecting general relativistic (GR) and magnetohydrodynamic (MHD) effects. As for GR effects, there have been several GR simulations that include detailed microphysics (e.g. Dimmelmeier et al. 2008; Sekiguchi 2010; Ott et al. 2012; Müller et al. 2013; Kuroda et al. 2014), which implied that GR leads to higher characteristic frequencies of gravitational wave signals due to more compact protoneutron stars as a consequence of stronger gravity. As for MHD effects, the magnetic fields would transfer the angular momentum from inside to outside and a strong jet is launched if the initial magnetic fields are strong enough, which would modify the GW signatures (Obergaulinger et al. 2006; Scheidegger et al. 2010; Takiwaki & Kotake 2011; Sawai et al. 2013). However, since MHD effects do not have a large impact around the bounce, our conclusion will not be affected even if we include magnetic fields in our simulation for future projects. Secondly, in this paper we employed one progenitor model, s11.2 of Woosley et al. (2002) because it is well studied by a number of previous works. It should be noted that the prompt convection depends on the structure of the progenitor model. Therefore, to assess the robustness of the results obtained in this study we need a more systematic study using multiple progenitor models. In addition, we employed one specific angular velocity distribution. More study of the dependence on the rotation profile is also needed (but see Abdikamalov et al. 2013). Finally, we did not take into account heavier leptonic neutrinos and neutrino oscillation effects. The height of the neutronization burst

should be smaller than the present estimation if we include neutrino oscillation effects. This issue will also be investigated in a forthcoming paper.

Acknowledgments

REFERENCES

Abbott, B. P., Abbott, R., Adhikari, R., et al. 2009, Reports on Progress in Physics, 72, 076901

Abdikamalov, E., Gossan, S., DeMaio, A. M., & Ott, C. D. 2013, ArXiv e-prints, arXiv:1311.3678

Abe, K., Abe, T., Aihara, H., et al. 2011, ArXiv e-prints, arXiv:1109.3262

Accadia, T., Acernese, F., Antonucci, F., et al. 2011, Classical and Quantum Gravity, 28, 114002

Adams, S. M., Kochanek, C. S., Beacom, J. F., Vagins, M. R., & Stanek, K. Z. 2013, ApJ, 778, 164

Alekseev, E. N., Alekseeva, L. N., Krivosheina, I. V., & Volchenko, V. I. 1987, 26, 237

Anderson, W. G., Brady, P. R., Creighton, J. D., & Flanagan, É. É. 2001, Phys. Rev. D, 63, 042003

Ando, S., & Sato, K. 2002, Progress of Theoretical Physics, 107, 957

Aso, Y., Michimura, Y., Somiya, K., et al. 2013, Phys. Rev. D, 88, 043007

Bahcall, J. N., Kamionkowski, M., & Sirlin, A. 1995, Phys. Rev. D, 51, 6146

Beacom, J. F., & Vagins, M. R. 2004, Physical Review Letters, 93, 171101

Bethe, H. A. 1990, Reviews of Modern Physics, 62, 801

Bethe, H. A., & Wilson, J. R. 1985, ApJ, 295, 14

Bionta, R. M., Blewitt, G., Bratton, C. B., Casper, D., & Ciocio, A. 1987, Physical Review Letters, 58, 1494

Bruenn, S. W., Mezzacappa, A., Hix, W. R., et al. 2013, ApJ, 767, L6

Buras, R., Janka, H., Rampp, M., & Kifonidis, K. 2006, A&A, 457, 281

Burrows, A. 2013, Reviews of Modern Physics, 85, 245

Burrows, A., & Hayes, J. 1996, Physical Review Letters, 76, 352

Burrows, A., Livne, E., Dessart, L., Ott, C. D., & Murphy, J. 2006, ApJ, 640, 878

Couch, S. M., & O'Connor, E. P. 2014, ApJ, 785, 123

Dimmelmeier, H., Ott, C. D., Marek, A., & Janka, H.-T. 2008, Phys. Rev. D, 78, 064056

Dolence, J. C., Burrows, A., & Zhang, W. 2014, ArXiv e-prints, arXiv:1403.6115

Epstein, R. 1978, ApJ, 223, 1037

Gando, A., Gando, Y., Hanakago, H., et al. 2012, Phys. Rev. C, 86, 021601

Grover, K., Fairhurst, S., Farr, B. F., et al. 2014, Phys. Rev. D, 89, 042004

Halzen, F., & Raffelt, G. G. 2009, Phys. Rev. D, 80, 087301

Handy, T., Plewa, T., & Odrzywołek, A. 2014, ApJ, 783, 125

Hanke, F., Marek, A., Müller, B., & Janka, H.-T. 2012, ApJ, 755, 138

Hanke, F., Müller, B., Wongwathanarat, A., Marek, A., & Janka, H.-T. 2013, ApJ, 770, 66

Hirata, K., Kajita, T., Koshiba, M., Nakahata, M., & Oyama, Y. 1987, Physical Review Letters, 58, 1490

Ikeda, M., Takeda, A., Fukuda, Y., et al. 2007, ApJ, 669, 519

Janka, H.-T. 2012, Annual Review of Nuclear and Particle Science, 62, 407

Jaranowski, P., Królak, A., & Schutz, B. F. 1998, Phys. Rev. D, 58, 063001

KAGRA official sensitivity. http://gwcenter.icrr.u-tokyo.ac.jp/researcher/parameters

Komatsu, E., Smith, K. M., Dunkley, J., et al. 2011, ApJS, 192, 18

Kotake, K., Takiwaki, T., Suwa, Y., et al. 2012, Advances in Astronomy, 2012, arXiv:1204.2330

Kuroda, K., & the LCGT Collaboration. 2010, Classical and Quantum Gravity, 27, 084004

Kuroda, T., Takiwaki, T., & Kotake, K. 2014, Phys. Rev. D, 89, 044011

Lattimer, J. M., & Swesty, F. D. 1991, Nuclear Physics A, 535, 331

Marek, A., & Janka, H. 2009, ApJ, 694, 664

Mohanty, S. D. 2002, Classical and Quantum Gravity, 19, 1513

Mönchmeyer, R., Schaefer, G., Müller, E., & Kates, R. E. 1991, A&A, 246, 417

Mori, T., ed. 2013, R &D project for Gd-doped water Cherenkov detector

Mueller, E., & Janka, H.-T. 1997, A&A, 317, 140

Müller, B., Janka, H.-T., & Marek, A. 2012, ApJ, 756, 84

—. 2013, ApJ, 766, 43

Nishino, H., Awai, K., Hayato, Y., et al. 2009, Nuclear Instruments and Methods in Physics Research A, 610, 710

Obergaulinger, M., Aloy, M. A., & Müller, E. 2006, A&A, 450, 1107

Ott, C. D. 2009, Classical and Quantum Gravity, 26, 063001

Ott, C. D., Burrows, A., Dessart, L., & Livne, E. 2008, ApJ, 685, 1069

Ott, C. D., Abdikamalov, E., O'Connor, E., et al. 2012, Phys. Rev. D, 86, 024026

Pagliaroli, G., Vissani, F., Coccia, E., & Fulgione, W. 2009, Physical Review Letters, 103, 031102

Sawai, H., Yamada, S., & Suzuki, H. 2013, ApJ, 770, L19

Scheidegger, S., Käppeli, R., Whitehouse, S. C., Fischer, T., & Liebendörfer, M. 2010, A&A, 514, A51

Sekiguchi, Y. 2010, Progress of Theoretical Physics, 124, 331

Suwa, Y. 2014, PASJ, 66, L1

Suwa, Y., Kotake, K., Takiwaki, T., Liebendörfer, M., & Sato, K. 2011, ApJ, 738, 165

Suwa, Y., Kotake, K., Takiwaki, T., et al. 2010, PASJ, 62, L49

Suwa, Y., Takiwaki, T., Kotake, K., et al. 2013, ApJ, 764, 99

Suwa, Y., Yamada, S., Takiwaki, T., & Kotake, K. 2014, ArXiv e-prints, arXiv:1406.6414

Takiwaki, T., & Kotake, K. 2011, ApJ, 743, 30

Takiwaki, T., Kotake, K., & Suwa, Y. 2012, ApJ, 749, 98

—. 2014, ApJ, 786, 83

Tomàs, R., Semikoz, D., Raffelt, G. G., Kachelrieß, M., & Dighe, A. S. 2003, Phys. Rev. D, 68, 093013

Totani, T., & Sato, K. 1995, Astroparticle Physics, 3, 367

Watanabe, H., Zhang, H., Abe, K., et al. 2009, Astroparticle Physics, 31, 320

Woosley, S. E., Heger, A., & Weaver, T. A. 2002, Reviews of Modern Physics, 74, 1015

Yokozawa, T. 2011, International Cosmic Ray Conference, 4, 90

Table 1: KAGRA detector coordinates.

parameter	value
latitude of KAGRA detector λ	$+36.41°$
longitude of KAGRA detector L	$+137.3°$
angle between East and bisector of the detector arms γ	$+75.0°$
angle between detector arms ζ	$90.0°$

Table 2: The distance dependence of GW, neutronization efficiency and P_r value for 0.0π rad/s model.

Distance[kpc]	GW eff.[%]	neutrino eff.[%]	detection eff.[%]	P_r[%]
0.1	71.9	100.0	71.9	0.0
0.2	61.1	100.0	61.1	0.0
0.3	52.5	100.0	52.5	0.4
0.4	44.5	100.0	44.5	3.1
0.5	39.6	100.0	39.6	8.6
0.6	34.2	99.4	33.9	14.8
0.7	29.9	93.0	27.6	21.3
0.8	25.3	78.6	20.1	22.8
0.9	22.7	58.6	13.6	28.0
1.0	19.2	42.2	8.3	28.0
1.5	7.3	6.3	0.4	35.6
2.0	1.9	1.3	<0.1	25.0

Table 3: The distance dependence of GW, neutronization efficiency and P_r value for 0.2π rad/s model.

Distance[kpc]	GW eff.[%]	neutrino eff.[%]	detection eff.[%]	P_r[%]
0.1	71.9	100.0	71.9	0.0
0.2	61.0	100.0	60.9	1.3
0.3	52.1	100.0	52.1	5.3
0.4	44.9	100.0	44.9	13.6
0.5	39.1	100.0	39.1	22.4
0.6	34.2	98.9	33.7	29.9
0.7	29.8	89.7	26.7	38.1
0.8	24.2	70.6	17.1	42.6
0.9	21.5	51.8	11.3	41.8
1.0	18.8	35.3	6.7	40.3
1.5	6.5	4.8	0.2	27.3
2.0	1.9	0.9	<0.1	0.0

Table 4: The distance dependence of GW, neutronization efficiency and P_r value for 0.5π rad/s model.

Distance[kpc]	GW eff.[%]	neutrino eff.[%]	detection eff.[%]	P_r[%]
0.1	84.9	100.0	84.9	0.2
0.2	77.7	100.0	77.7	1.8
0.3	73.7	100.0	73.7	8.5
0.4	69.6	100.0	69.6	17.1
0.5	65.1	100.0	65.1	26.1
0.6	62.8	99.0	62.2	33.9
0.7	60.3	91.4	55.5	40.0
0.8	56.6	75.0	42.8	44.0
0.9	54.1	55.1	29.7	48.0
1.0	52.5	38.8	20.3	47.3
1.5	43.0	6.1	2.6	45.6
2.0	35.1	1.1	0.3	35.5

Table 5: The distance dependence of GW, neutronization efficiency and P_r value for 1.0π rad/s model.

Distance[kpc]	GW eff.[%]	neutrino eff.[%]	detection eff.[%]	P_r[%]
0.1	87.2	100.0	87.2	95.8
0.2	82.0	100.0	82.0	92.6
0.3	78.3	100.0	78.3	90.1
0.4	74.6	100.0	74.6	88.6
0.5	72.3	100.0	72.3	86.8
0.6	69.6	98.1	68.1	87.3
0.7	67.4	87.0	58.6	87.0
0.8	65.1	68.0	44.5	85.7
0.9	63.0	49.1	30.7	85.9
1.0	61.0	34.1	20.9	85.8
1.5	52.8	5.7	3.2	83.8
2.0	45.8	1.3	0.7	69.6
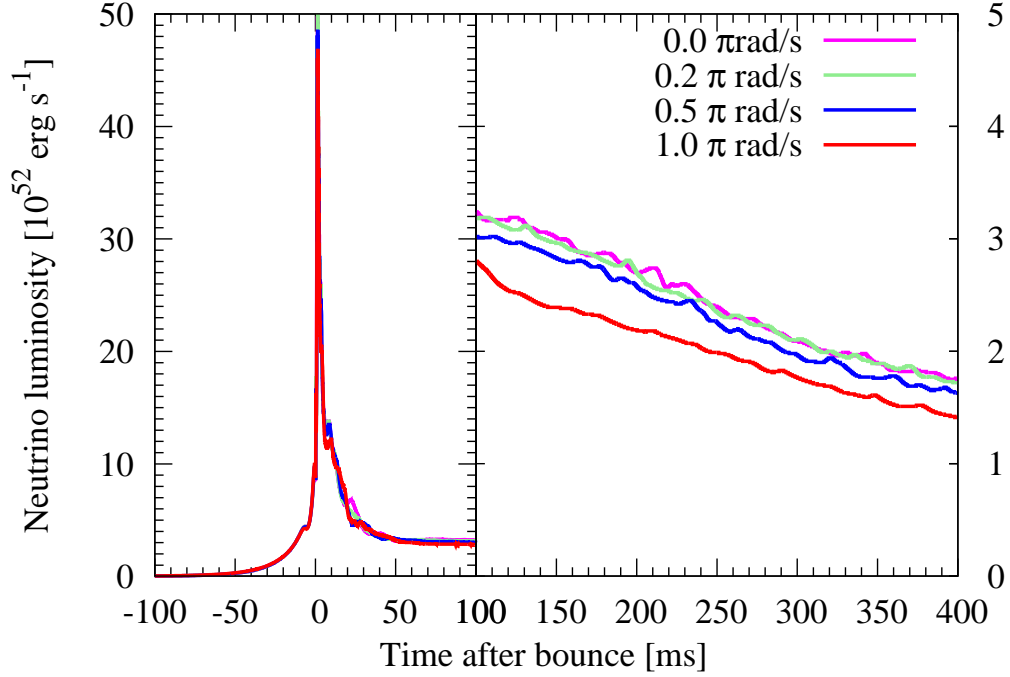
(a) ν_e
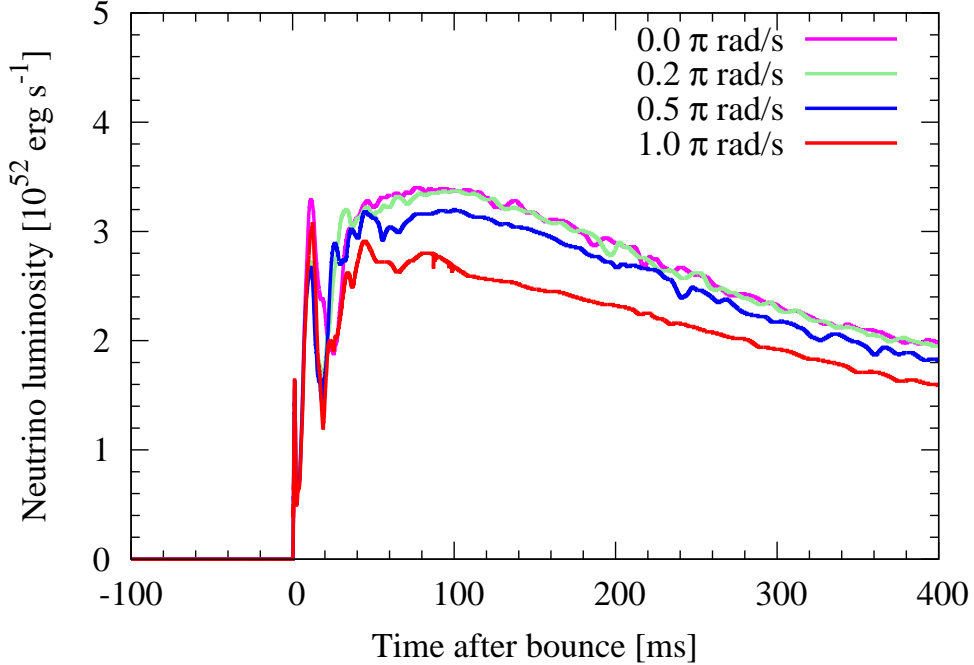
(b) $\bar{\nu}_e$

Fig. 1.— Time evolution of luminosities of electron-type neutrinos (ν_e; panel(a)) and antineutrinos ($\bar{\nu}_e$; panel (b)). Each line represents models with different initial rotation rates, i.e., no rotation($\Omega_0 = 0.0\pi$) (magenta), $\Omega_0 = 0.2\pi$ rad s^{-1} (green), $\Omega_0 = 0.5\pi$ rad s^{-1} (blue), and $\Omega_0 = 1.0\pi$ rad s^{-1} (red), respectively. Note that left and right sides in panel (a) have different scales.
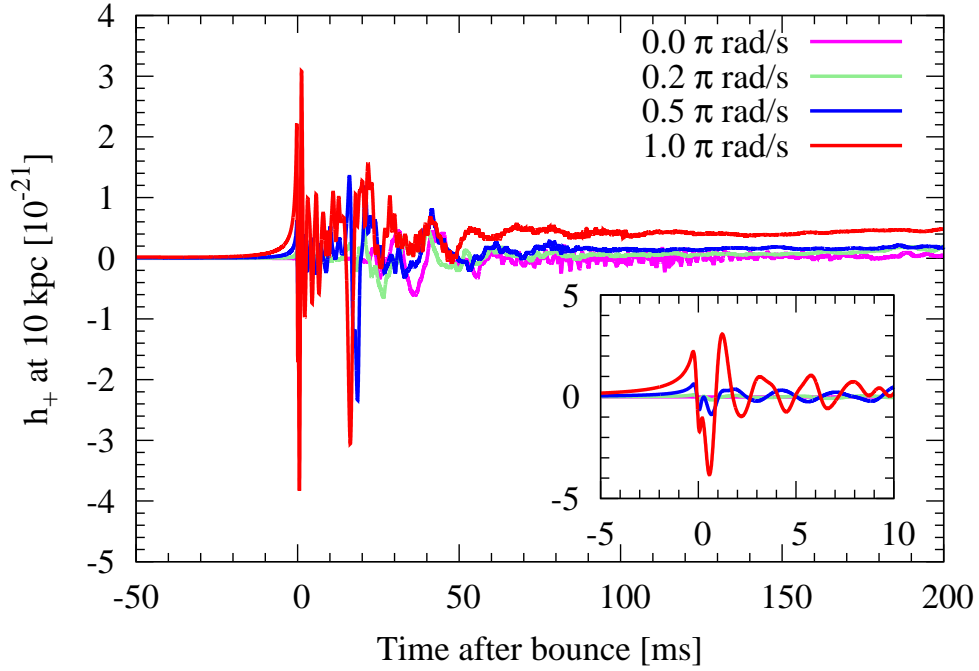
Fig. 2.— GW amplitude as a function of time for a core-collapse supernova occurring 10 kpc from the observer. Each line represents models with different initial rotation rate, i.e., no rotation ($\Omega_0 = 0.0\pi$) (magenta), $\Omega_0 = 0.2\pi$ rad s^{-1} (green), $\Omega_0 = 0.5\pi$ rad s^{-1} (blue), and $\Omega_0 = 1.0\pi$ rad s^{-1} (red), respectively. The small panel shows features around the bounce time. The fast rotation model exhibits a large amplitude GW at the bounce, while the slow rotation models have very small amplitudes. Since the later phase (i.e., a few tens of ms after the bounce) activity is dominated by convection motion, all models imply similar amplitude in the later phase.
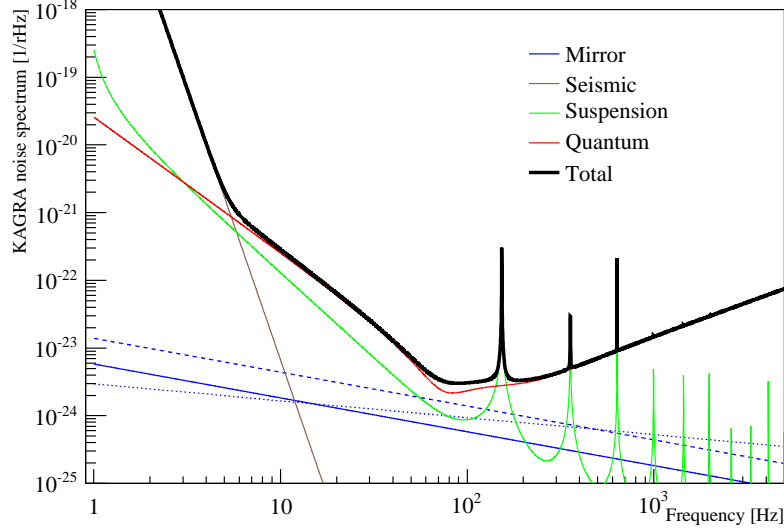
Fig. 3.— KAGRA official sensitivity curve. These curves are estimated from an incoherent sum of the fundamental noise sources. The colors show each type of environmental noise and the black line shows total noise. Blue lines are mirror related noise, brown shows seismic noise, green shows suspension thermal noise, and red shows quantum noise, respectively.
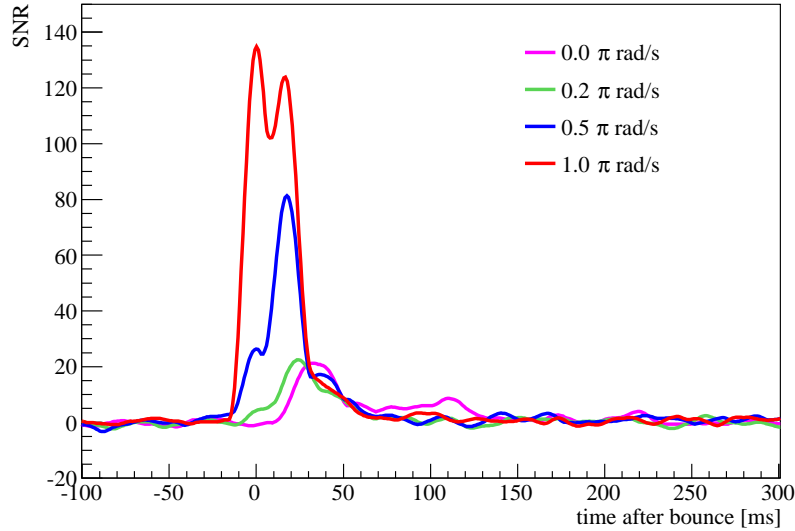
Fig. 4.— One example of the time variation of obtained SNR for each model. Each color shows one progenitor core rotation model, 0.0π(magenta), 0.2π(green), $0.5\pi$(blue) and 1.0π(red) rad s^{-1}, respectively. The supernova distance is set to 1.0 kpc and on-direction for the KAGRA detector.
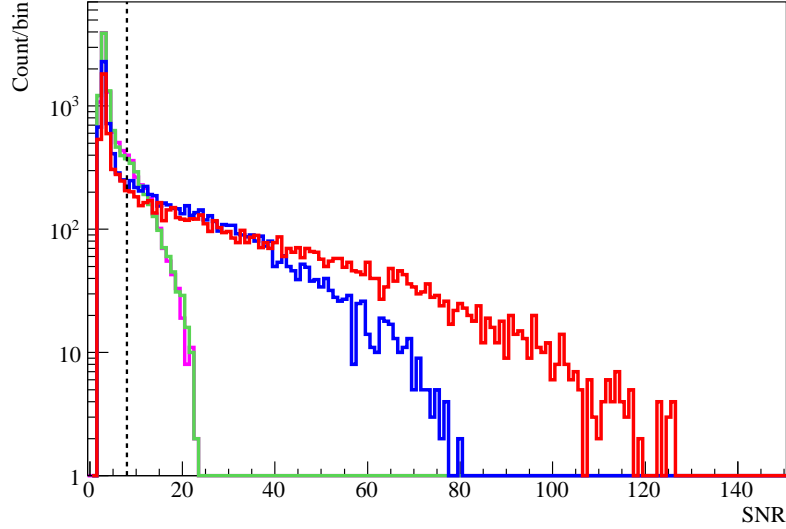
Fig. 5.— The max SNR distribution for each model. The supernova distance from Earth is fixed at 1kpc and direction is randomly distributed. Each color shows one progenitor core rotation model, 0.0π(magenta), 0.2π(green), 0.5π(blue) and 1.0π(red) rad s^{-1}, respectively. The black line shows the detection threshold, which corresponds to max SNR>8.
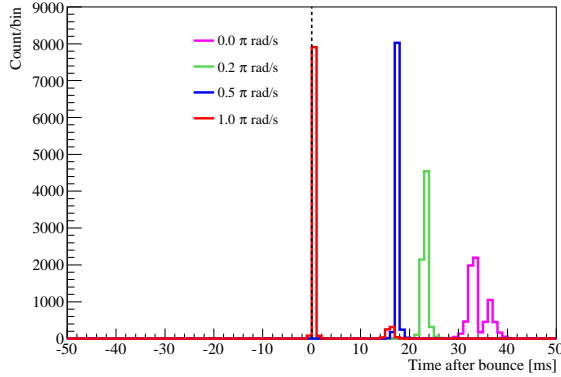
Fig. 6.— The T$_{GW}$ extracted start time distribution of GW emission for each explosion model. The distance is fixed at 0.1kpc. Horizotal axis shows time from core bounce. Each color shows one progenitor core rotation model, 0.0π(magenta), 0.2π(green), 0.5π(blue) and 1.0π(red) rad s^{-1}, respectively.
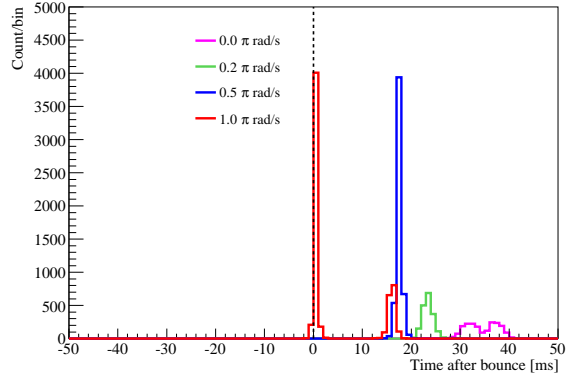
Fig. 7.— The T$_{GW}$ distribution of GW emission for each explosion model. The distance is fixed at 1.0 kpc. Horizotal axis shows time from core bounce. Each color shows one progenitor core rotation model, 0.0π(magenta), 0.2π(green), 0.5π(blue) and 1.0π(red) rad s^{-1}, respectively.
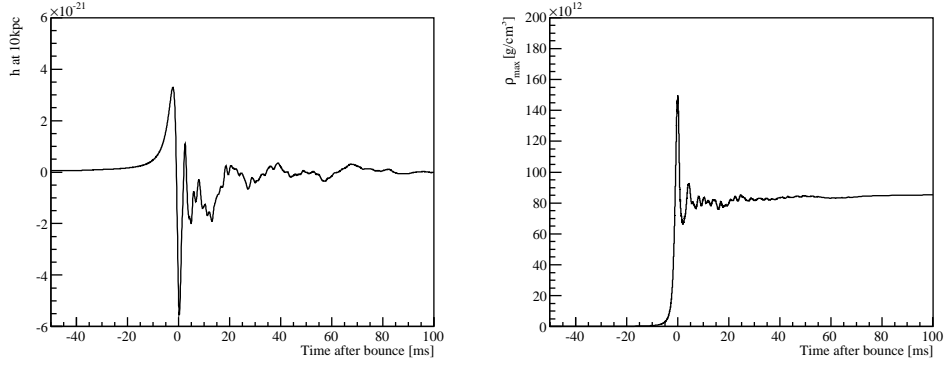
Fig. 8.— One example of the Dimmelmeier model, e20b-ls in the paper(Dimmelmeier et al. 2008). (Left) Time variation of gravitational wave amplitude h as a function of time from core bounce for 10 kpc. (Right) Time variation of maximum density ρ_{max}.
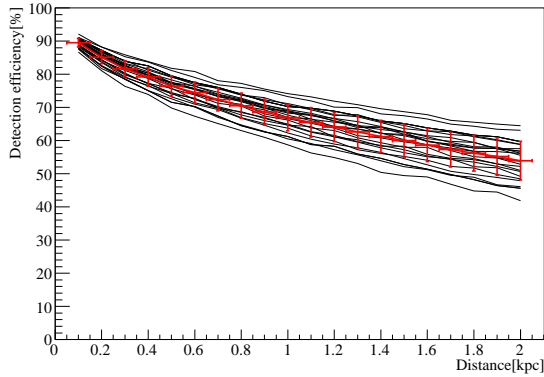
Fig. 9.— The distance dependence of the detection efficiency for Dimmelmeier 25 models. Black lines show each model and red points show mean value and one sigma expansion of these models for each distance.
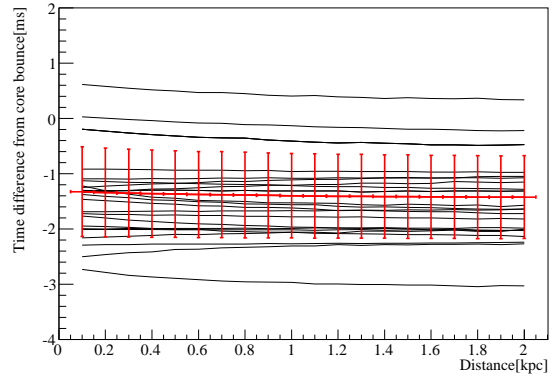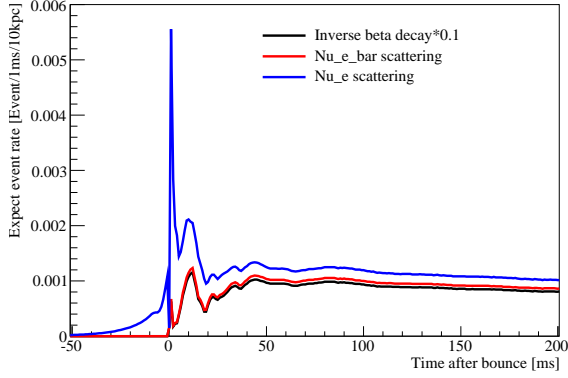
Fig. 10.— The distance dependence of the time difference from core bounce time for Dimmelmeier 25 models. Black lines show for each model and red points show mean value and one sigma expansion of these models for each distance.

Fig. 11.— Expected number of interactions in EGADS. Black component shows electron neutrino-electron elastic scattering, blue component shows electron anti-neturino-electron elastic scattering, and red component shows 10% of inverse beta decay interaction. Horizontal axis shows time and vertical axis shows unit of event/1ms/10kpc.
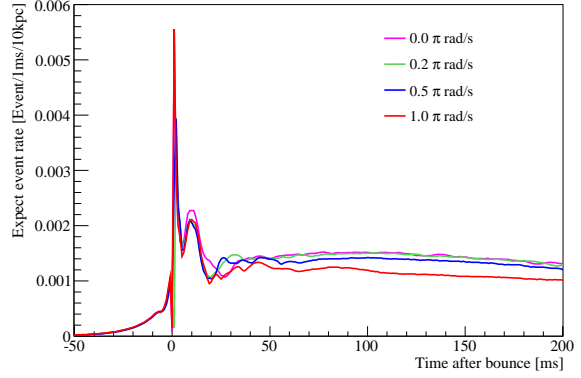
Fig. 12.— Model dependence of expected number of summed interaction in EGADS. Each color shows one progenitor core rotation model, 0.0π(magenta), 0.2π(green), 0.5π(blue) and 1.0π(red) rad s^{-1}, respectively. Horizontal axis shows time and vertical axis is the sum of expected interactions in EGADS in units of event/1ms/10kpc.
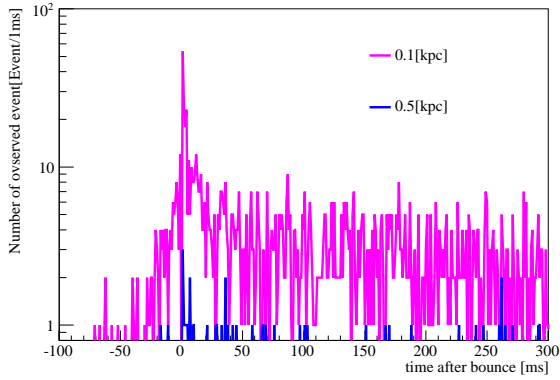
Fig. 13.— One example of the fluctuation of observed number of neutrinos for the distance 0.1 kpc(red) and 0.5 kpc(blue). The 1.0 πrad s^{-1} model is used for this figure.
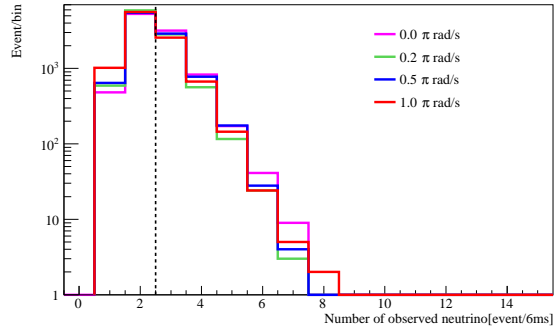

Fig. 14.— The number of maximum observed neutrinos used as threshold. Colors show the progenitor core rotation models, 0.0π(magenta), 0.2π(green), 0.5π(blue) and 1.0π(red) rad s^{-1}, respectively. Horizontal axis is number of observed events.
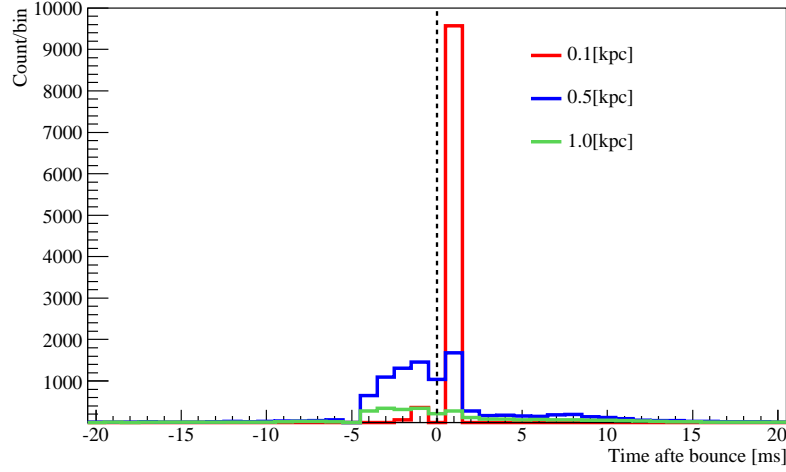
Fig. 15.— The obtained T_ν distribution in case of 0.1 kpc(red), 0.5 kpc(blue) and 1.0 kpc(green).
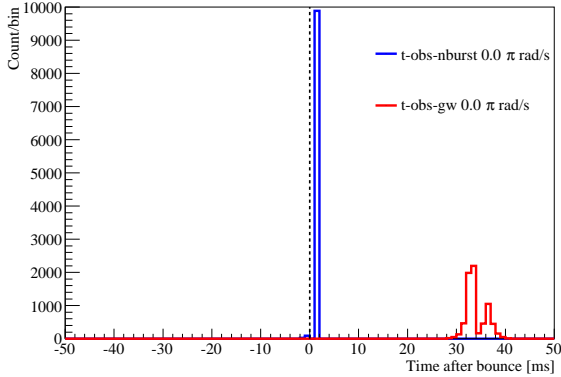

Fig. 16.— Time comparison between T_{GW}(red) and T_ν(blue) distribution for 0.0π rad s^{-1} model. The distance is fixed at 0.1 kpc. Both GW and neutrino distributions are made after applying detection threshold. Horizontal axis shows time from core bounce.
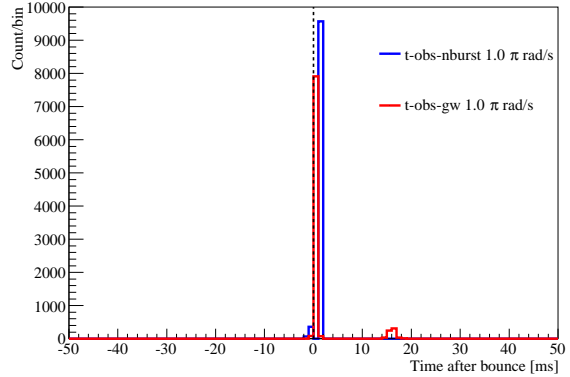
Fig. 17.— Time comparison between T_{GW}(red) and T_ν(blue) distribution for 1.0π rad s^{-1} model. The distance is fixed at 0.1 kpc. Both GW and neutrino distributions are made after applying detection threshold. Horizontal axis shows time from core bounce.
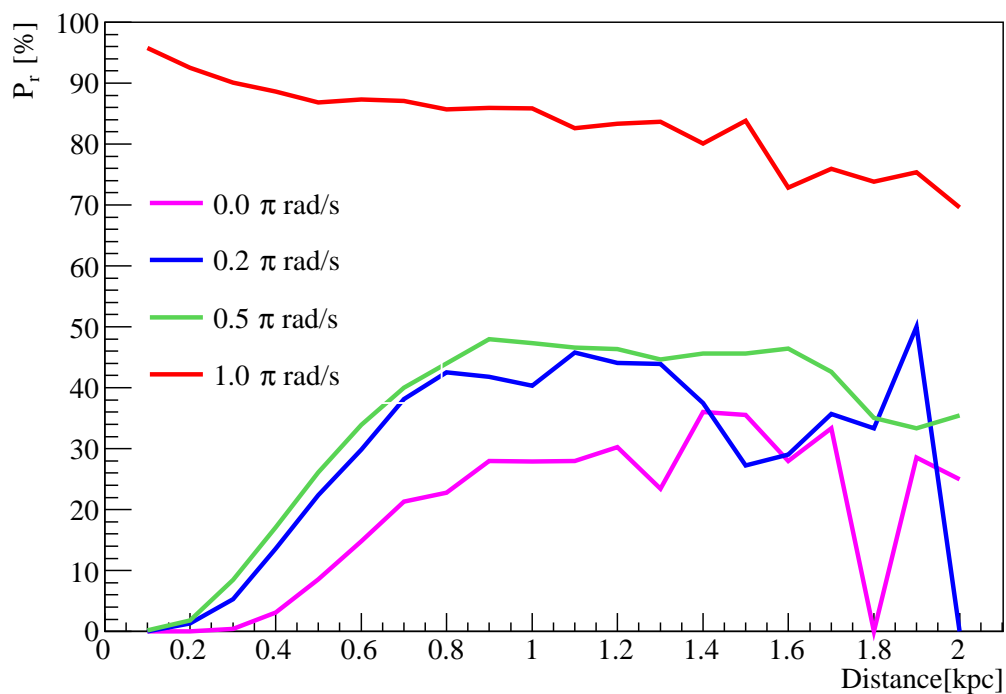
Fig. 18.— Model dependence of P$_r$ distribution, which is the probability of core rotation. Horizotal axis shows distance. Each color shows one progenitor core rotation model, 0.0π(magenta), 0.2π(green), 0.5π(blue) and 1.0π(red) rad s^{-1}, respectively.